

WASP-35 and HAT-P-30/WASP-51: re-analysis using TESS and ground-based transit photometry

LU BAI,^{1,2,3,*} SHENGHONG GU,^{1,2,4} XIAOBIN WANG,^{1,2,4} LEILEI SUN,^{1,2,*} CHI-TAI KWOK,⁵ AND HO-KEUNG HUI⁵

¹*Yunnan Observatories, Chinese Academy of Sciences, Kunming 650216, China*

²*Key Laboratory for the Structure and Evolution of Celestial Objects, Chinese Academy of Sciences, Kunming 650216, China*

³*University of Chinese Academy of Sciences, Beijing 100049, China*

⁴*School of Astronomy and Space Science, University of Chinese Academy of Sciences, Beijing 101408, China*

⁵*Ho Koon Nature Education cum Astronomical Centre, Sik Sik Yuen, Hong Kong, China*

ABSTRACT

High-precision transit observations provide excellent opportunities for characterizing the physical properties of exoplanetary systems. These physical properties supply many pieces of information for unveiling the internal structure, external atmosphere, and dynamical history of the planets. We present revised properties of transiting systems WASP-35 and HAT-P-30/WASP-51 through analyzing newly available TESS photometry and ground-based observations obtained at 1m telescope of Yunnan Observatories as well as from the literature. The improved system parameters are consistent with the previous results. Furthermore, we find that HAT-P-30b/WASP-51b's transits show significant timing variation which cannot be explained by decaying orbit due to tidal dissipation and the Rømer effect, while both apsidal precession and an additional perturbing body could reproduce this signal through our comprehensive dynamical simulations. Because both of them are valuable targets which are suitable for transmission spectroscopy, we make some predictions for atmospheric properties of WASP-35b and HAT-P-30b/WASP-51b based on newly derived system parameters.

Keywords: Exoplanet systems (484) — Transit photometry(1709) — Transit timing variation method(1710) — Gaussian Processes regression (1930) — Markov chain Monte Carlo (1889)

1. INTRODUCTION

Transiting exoplanets have been playing a fundamental role in revolutionizing the planetary science for more than two decades. High precision photometry during the transits and spectroscopic measurements provide perfect opportunities to characterize the physical properties of transiting exoplanetary systems. These information give the first hints about the internal structure, external atmosphere, and dynamical history of the planetary systems. Therefore, it is important to enlarge the number of the exoplanetary systems with accurately measured physical properties aiming to the statistically analyze as well as establish the formation and evolution models of planetary systems.

Long-term transit monitoring observations and thus physical properties updating for known transiting exoplanetary systems are essential for discovering additional bodies and scheduling further observations. A single transiting planet generally orbits around its host star on a Keplerian orbit with a constant orbital period in the timescale of years, in which the influence of tidal effect and general relativity effect can be negligible due to no effective accumulation. But the transit timing variations (TTV; Agol et al. 2005; Holman & Murray 2005), which means transits no longer appear at a fixed interval, would exist in principle if there are additional bodies in the planetary systems. In some cases the gravitational interaction between planets will trigger relatively short-term TTVs (Agol et al. 2005; Holman & Murray 2005). The patterns of these TTVs (e.g., amplitude, frequency, and overall shape) strongly rely on the orbital parameters and masses of the planets involved (see e.g. Agol et al. 2005; Holman & Murray 2005; Nesvorný & Morbidelli 2008; Lithwick et al. 2012; Xie et al. 2014). As the gravitational interactions among planets that induce

Corresponding author: wangxb[at]ynao[dot]ac[dot]cn (XBW), sunleile[at]ynao[dot]ac[dot]cn (LLS)

* Lu Bai and Leilei Sun contributed equally to this work.

the TTVs generally act on timescales much longer than the orbital periods, space-based transit survey missions, such as *Kepler* and upcoming PLATO, and ground-based follow-up transit monitoring with longer baselines are more likely to capture such phenomena (Mazeh et al. 2013; Rowe et al. 2014; Holczer et al. 2016). Furthermore, TTV technique is a powerful tool for understanding planetary systems: it can place a constraint on the existence of non-transiting exoplanets, thereby remedying missing pieces to the architecture of the systems due to the geometry bias which is inherent to the transit method (Xie et al. 2014; Zhu et al. 2018; Sun et al. 2021), and allowing for a better comparison with synthetic planetary system population models (see e.g. Mordasini et al. 2009; Mordasini 2018; Wu et al. 2019). On the other hand, TTVs can also be used to measure the masses of the planets (see e.g. Nesvorný et al. 2012; Lithwick et al. 2012), and therefore their density, which hence place strong constraints on their internal structures, such as the cases for Kepler-411 system (Sun et al. 2019), Trappist-1 system (Grimm et al. 2018; Agol et al. 2021) and so on. Detection of individual dynamically hot systems also provides valuable constraints on planetary system formation theory, as the current orbit of a system can remain the information of its past migration history (see e.g. Delisle 2017; Nesvorný et al. 2021).

In addition, there are many exoplanetary systems show temporal variations in their orbital properties, several reasons may cause the change in orbital properties, such as the long-term effects of tidal forces, the elliptical orbit precession, mass loss, and so on; these mechanisms may mimic above mentioned TTVs generated by the gravitational interactions with other bodies. Among these cases, orbital decay induced by tidal dissipation is another most interesting one besides the gravitational interactions with other bodies, relative theory suggests it tends to occur in planets with shorter orbital periods and larger masses; such kind of TTV signals of hot giant planets could also be used to constrain the planetary tidal quality factor and study the dynamical history of planetary systems (Goldreich & Soter 1966). While, direct observational evidences still remain sparse, further investigations will improve our understanding on the dynamical history of planetary systems. Fortunately, both space- and ground-based transit photometry can be used to search for TTVs, this will accumulate a lot of data and valuable targets.

To refine physical properties and investigate the TTV behaviour of known transiting exoplanetary systems, both ground- and space-based transiting light curves are necessary. Since 2009, we have monitored the transit events of some known transiting exoplanetary systems by employing the 1m telescope of Yunnan Observatories (hereafter, YO-1m) in China, and obtained a series of high-precision photometric data (see e.g. Tan et al. 2013; Wang et al. 2013, 2014; Sun et al. 2015, 2017). For the ground-based transit observations, the most challenging thing is the systematic noise due to the variable atmosphere of the Earth, so some noise reduction techniques (Collier Cameron et al. 2006; Tamuz et al. 2005; Carter & Winn 2009; Rasmussen & Williams 2006; Gibson et al. 2012; Wilson et al. 2021) have been developed and widely used to handle this issue. Moreover, the Transiting Exoplanet Survey Satellite (TESS; Ricker et al. 2014, 2015) has been producing high quality transiting light curves which are well suited for refining the physical properties of known planetary systems.

Here we focus on the planetary systems WASP-35 and HAT-P-30. Both of them had been observed by TESS in two sectors, and we also observed one transiting event for each system using YO-1m. Based on these light curves and radial velocity (RV) data from the literature, we refined their system parameters, analyzed the TTVs of these planetary systems, and made predictions about the atmospheric properties of them based on our refined physical parameters. We give a short introduction of the targets in Section 2. Then we describe the observations and data reduction in Section 3, and present the modeling in Section 4. The further analysis and discussion is given in Section 5. At last, we summarize the study in Section 6.

2. TARGETS

2.1. WASP-35

WASP-35b was discovered by Enoch et al. (2011) in the Wide Angle Search for Planet (WASP) project. This transiting exoplanet system has a inflated ($M_p = 0.72 \pm 0.06 M_{Jup}$ and $R_p = 1.32 \pm 0.05 R_{Jup}$) hot Jupiter which orbits a metal-poor ($[Fe/H] = -0.15 \pm 0.09$) host star with a period of 3.16 days. Through analyzing their photometric and spectroscopic observations at a series of ground-based telescopes, Enoch et al. (2011) confirmed the planetary nature of WASP-35b and suggested that the host star of WASP-35 was lack of stellar activity. Later, Mortier et al. (2013, 2014) updated the physical parameters of the host star using a spectroscopic analysis, Kokori et al. (2021) re-analyzed and updated the ephemeris based on the light curves of Enoch et al. (2011), and Shan et al. (2021) refined and updated the ephemeris using the data of TESS photometry.

2.2. HAT-P-30

HAT-P-30b (also known as WASP-51b) was discovered independently by ? in the Hungarian-made Automatic Telescope Network (HATNet) and Enoch et al. (2011) in the WASP project, respectively. HAT-P-30b is a transiting hot Jupiter ($M_p = 0.711 \pm 0.028 M_{Jup}$ and $R_p = 1.340 \pm 0.065 R_{Jup}$) orbiting a late F-type host star with a period of 2.81 days and the orbit is circular. HAT-P-30 has a relatively bright ($V=10.4$) host star, therefore it is very suitable for using transmission spectra to study the planetary atmosphere. ? studied the Rossiter-McLaughlin effect of HAT-P-30 system, and found the orbit of HAT-P-30b was highly tilted with a sky-projected angle between the star’s spin axis and the planet’s orbit normal, $\lambda = 73.5 \pm 9.0^\circ$. Maciejewski et al. (2016), Saha et al. (2021), Wang et al. (2021) and Edwards et al. (2021) acquired new transit light curves of HAT-P-30b based on several ground-based telescopes and measured the physical parameters. Davoudi et al. (2020) analyzed several relative high quality transit light curves of HAT-P-30b collected from the Exoplanet Transit Database (ETD) ¹. Kokori et al. (2021) re-analyzed and updated the ephemeris based on the light curves of Maciejewski et al. (2016), ? and Enoch et al. (2011), and found no TTVs for HAT-P-30b.

3. OBSERVATIONS AND DATA REDUCTION

3.1. TESS photometry

TESS is an all-sky space survey, which is designed to search for transiting exoplanets orbiting the bright and nearby stars, these planet systems are enable us to carry out the follow-up observations and study their physical properties. TESS performs time-series photometry to monitor at least 200,000 main-sequence stars using four 100 mm telescopes with wide-field optical CCD cameras. The broad passband filter of TESS covers from 600 to 1000 nm and the combined field of view of each sector is 24×96 square degrees. Since its launch in 2018, TESS has completed 44 sectors of observations and collected a lot of high-quality transiting light curves.

WASP-35 was observed by TESS in Sectors 5 (2018 November 15 - 2018 December 11) and Sectors 32 (2020 November 19 - 2020 December 17), and HAT-P-30 was observed by TESS in Sectors 7 (2019 January 7 - 2019 February 2) and Sectors 34 (2021 January 13 - 2021 February 9). The data were collected in a 2 minute cadence and reduced by the pipeline developed by the Science Processing Operations Center (SPOC; Jenkins et al. 2016). We downloaded the light curve files from the archives at Mikulski Archive for Space Telescopes (MAST)² and accessed the light curves using the **Lightkurve** python package (Lightkurve Collaboration et al. 2018). These data had been corrected for the instrumental systematic variations by using the SPOC pipeline, but some long-term trends still remained in the data. In order to alleviate the influences from the remaining trends, we employed Gaussian Process (GP; Rasmussen & Williams 2006) to model these data (see below for further details). At last, we obtained 15 complete transit light curves of WASP-35 and 16 complete transit light curves of HAT-P-30. The time system of these light curves is barycentric Julian date (BJD) which can be used directly to determine the system parameters and ephemerides. The examples of raw TESS light curves are displayed in the top panels of Figure 1 and Figure 2, respectively.

3.2. Ground-based photometry

We observed the transit events of WASP-35 and HAT-P-30 using the Andor 4K×4K CCD camera attached to the YO-1m on 2018 November 20 and 18, respectively. The Johnson-Cousins R filter was utilized in both observations and the field of view is 15×15 arcmin². During two observations, both weather conditions and instrument statuses were good, and the exposure times were 120s. The transit event of HAT-P-30b occurred at sunset, which resulted in a relatively larger dispersion at the beginning of the observation (see Figure 3). In addition, we collected two sets of high quality light curves of HAT-P-30 from the CDS database, these light curves were observed by ? using the KeplerCam imager of the 1.2 m telescope at the Fred Lawrence Whipple Observatory (FLWO-1.2m).

The data reduction follows the standard procedures which were described in Wang et al. (2013). Our data reduction pipeline is based on the IRAF package, written in the python language by means of the pyRAF interface, including image checking, image trimming, bias subtraction, flat-field correction, cosmic ray removal, establish astrometric solution, aperture photometry and systematic error correction. To reach a higher precision, the pipeline attempts a series of photometric apertures for the target and reference stars and we pick out an optimal one to minimize the dispersion of each light curve. The transit light curve is obtained by using the optimal aperture.

¹ <http://var2.astro.cz/ETD/>

² <https://archive.stsci.edu/mission/tess/>

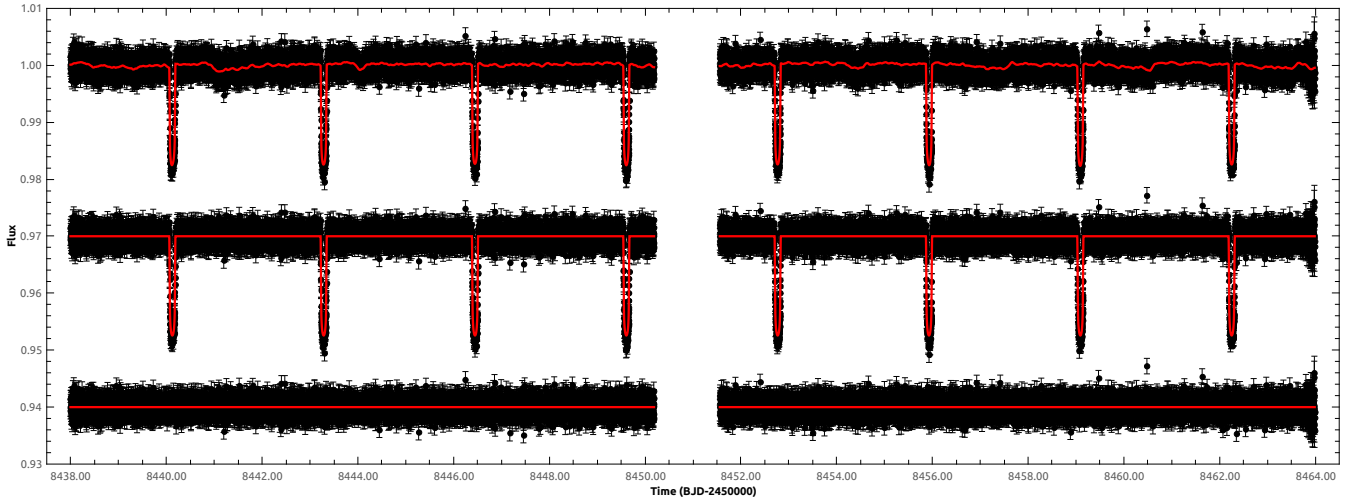


Figure 1. Transit light curves of WASP-35 observed by TESS in Sectors 5. The top is raw light curves with the best-fitting transit + noise model, the middle is the detrended light curves with the best-fitting transit model, and the bottom is the corresponding residuals. Vertical shifts are added for visualization.

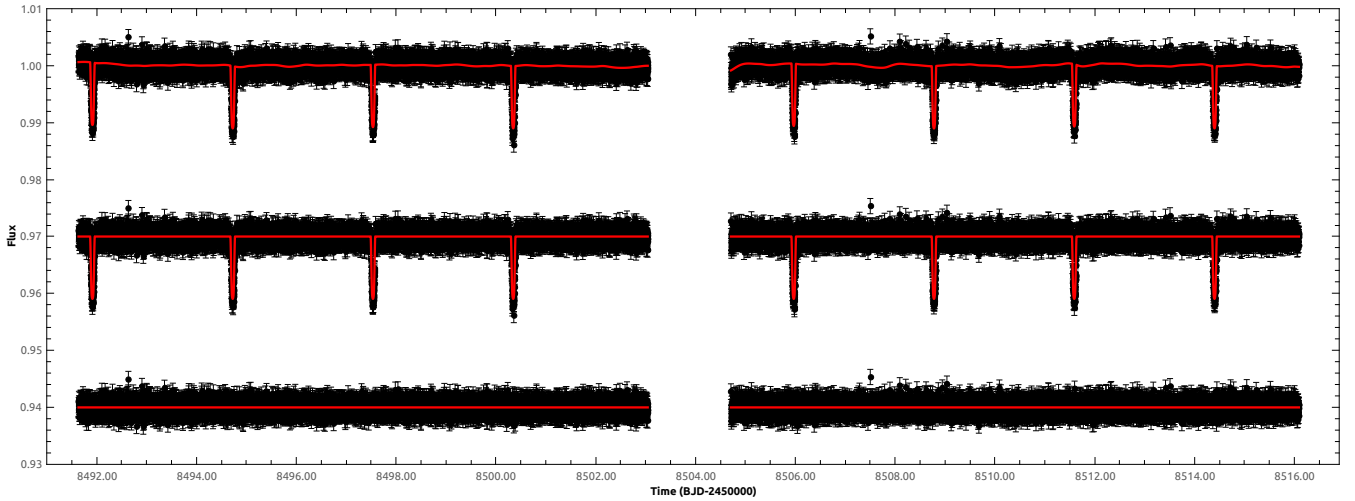


Figure 2. Transit light curves of HAT-P-30 observed by TESS in Sectors 7. The top is raw light curves with the best-fitting transit + noise model, the middle is the detrended light curves with the best-fitting transit model, and the bottom is the corresponding residuals. Vertical shifts are added for visualization.

For the ground-based observations, the shallow transit signals are easy to be drowned out by the systematic errors due to the effect of the telluric atmosphere and imperfect observation conditions, so it is necessary to remove the systematic errors hiding in above transit light curves. First, we employed the coarse de-correlation (Collier Cameron et al. 2006) and SYSREM algorithms (Tamuz et al. 2005) to diagnose and correct them by using the pipeline mentioned above. At this point, there are still some long-term systematic trends in the transit light curves, we employed GP to diagnose and correct them. Furthermore, in order to obtain accurate ephemerides of targets, we converted the observing time into barycentric Julian date by using the method proposed by Eastman et al. (2010).

3.3. Gaussian Processes

Gaussian Process (Rasmussen & Williams 2006) is a popular method which has been widely used to model time series data in the exoplanet community for about a decade, such as modeling stellar activity signals in RV data and correcting instrumentally induced systematic errors in transit light curves (Gibson et al. 2012; Evans et al. 2015; Murgas et al. 2020; Hurt et al. 2021; Langellier et al. 2021). Instead of modeling instrumental systematic errors as a deterministic function with auxiliary measurement parameters, GP provides a non-parametric method to model systematic errors

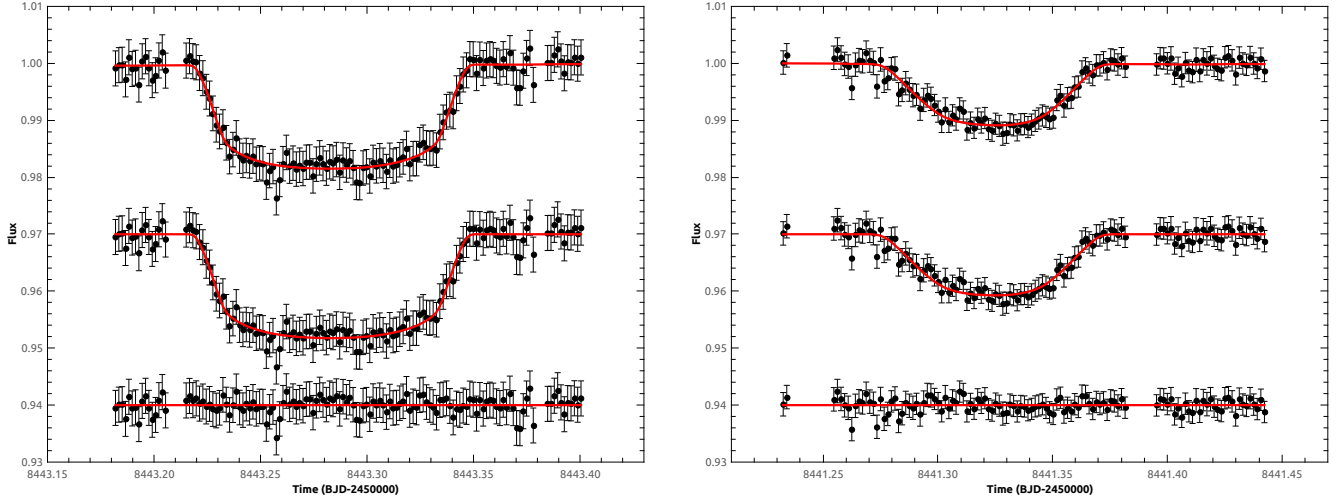


Figure 3. The transit light curves of WASP-35 (left panel) and HAT-P-30 (right panel) observed using YO-1m. The top row is raw light curves with the best-fitting transit + noise model, the middle row is light curves removed the noise with the best-fitting transit model, and the bottom row is the corresponding residuals.

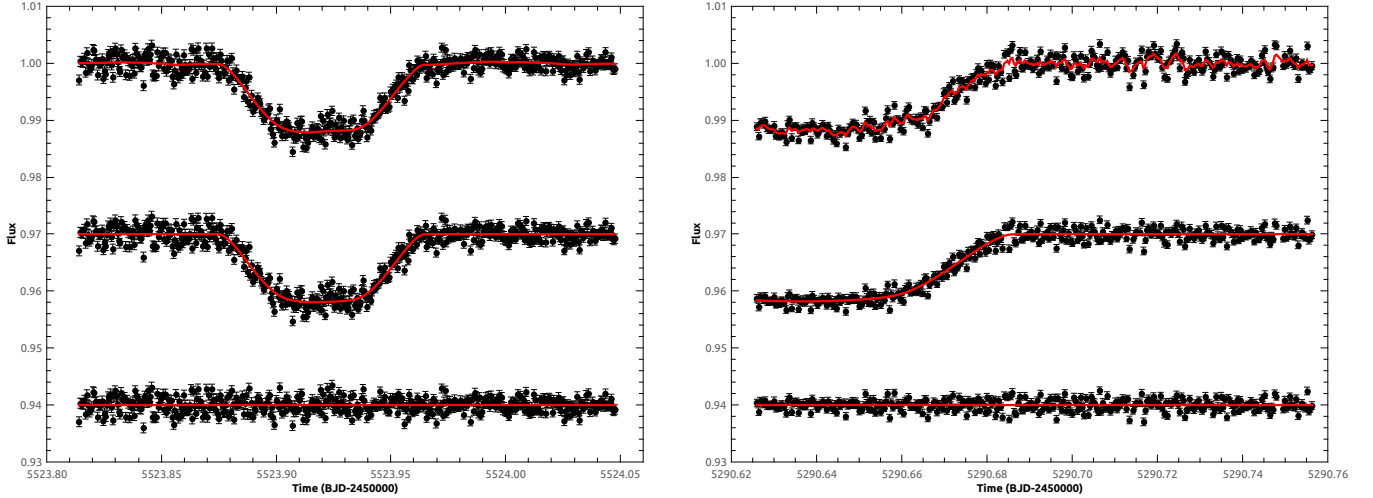


Figure 4. The transit light curves of HAT-P-30 observed using FLWO-1.2m. The top row is raw light curves with the best-fitting transit + noise model, the middle row is light curves removed the noise with the best-fitting transit model, and the bottom row is the corresponding residuals.

from the observed data set. Here, we used the code of **juliet** (Espinoza et al. 2019) to corrected long-term trends and instrumental systematic errors in TESS photometry data and the residual systematic errors in the ground-based photometry data.

We modeled the photometric light curves in flux space separately depending on the instrument and the time of the observation by using **juliet** code. For the photometry data sets, **juliet** establishes a common model in which light curve is modeled as a linear combination of the transit model and the noise model:

$$\mathcal{M}(t) + \epsilon(t)$$

where $\mathcal{M}(t)$ is the transit model with the dilution factor for the given instrument and the mean offset of out-of-transit flux, $\epsilon(t)$ is the noise model which is being modeled by GP in the photometric light curve. **Juliet** uses the analytic transit light curve model of Mandel & Agol (2002) with a quadratic limb-darkening law and the limb-darkening coefficients (q_1 and q_2) proposed by Kipping (2013) to model the transit signals and employs **batman** package (Kreidberg 2015) to implement the transit light curve model.

We checked the nearby stars around WASP-35 and HAT-P-30 using Gaia DR3 database (Gaia Collaboration et al. 2021), both of the fields do not seem to be especially crowded, and there was no other source bright enough to make a perceptible impact, so we fixed the dilution factors of both of the targets to 1. For TESS photometry data, the state of the instrument may be different in different observation sectors, so we modeled the TESS data sector by sector, respectively. For the ground-based observations, the state of ground-based instrument and the weather is changing from day to day, so we modeled the ground-based data day by day, respectively. In all of the model processes, we chose a celerite (approximate) Matern multiplied exponential kernel within **Juliet** implemented by **celerite** package (Foreman-Mackey et al. 2017). For the analytic transit model part, the parameters are the orbital period P , the mid-transit time T_0 , scaled semi-major axis a/R_A , the eccentricity e (fixed to 0), the argument of periastron ω (fixed to 90 degrees), the impact parameter b , the planet-to-star radius ratio R_b/R_A , the limb-darkening coefficients q_1 and q_2 , the mean out-of-transit flux, the dilution factors (fixed to 1), and the jitter. The input values we used were obtained by Enoch et al. (2011) for WASP-35 and ? for HAT-P-30 respectively, and a wide normal prior was used in the GP. For the GP component, the hyperparameters were the amplitude of the GP, two length scales corresponded to the Matern and the exponential part. We used a log-uniform prior for these hyperparameters, the amplitude of the GP varied from 10^{-6} to 10^6 , and both of the two length scales varied from 10^{-3} to 10^3 . **Juliet** uses **PyMultiNest** package (Buchner et al. 2014; Feroz et al. 2009) with 500 live points to explore the parameter space. Finally, we obtained the raw light curves and the full median posterior model, namely the transit model plus the median GP process. So we could subtract the GP part of the model from the raw light curve to correct the residual systematic errors in photometry data and obtained the final light curves. The transit light curves before and after the GP correction with the best-fitting models and the residuals are shown in Figure 1, Figure 2, Figure 3 and Figure 4.

4. TRANSIT AND RV MODELING

We used the Markov Chain Monte Carlo (MCMC) technique to fit the final light curves and the RV curves of Enoch et al. (2011) and ? simultaneously, and derived the system parameters as well as the ephemerides for further analysis (Collier Cameron et al. 2007; Pollacco et al. 2008). The code which we employed to model the transit light curves and RV curves was developed by Collier Cameron et al. (2007), which is based on the analytic transit light curve model proposed by Mandel & Agol (2002) associating with the four-coefficient limb-darkening law. The input parameters include: the orbital period P , the mid-transit time T_0 , the transit duration t_T , the planet to star area ratio ΔF , the impact parameter b , the semi-amplitude of the RV curve K_1 , the orbital eccentricity e and the argument of periastron ω . In order to accelerate the convergence of the system parameters, $e \cos \omega$ and $e \sin \omega$ are used to replace e and ω in the MCMC processes. The mass and radius of host stars were derived from the calibration for stellar masses and radii proposed by Enoch et al. (2010), which is based on the stellar effective temperature, metallicity and density. The limb-darkening coefficients were obtained by interpolating the coefficient tables of Claret (2000, 2004) according to the stellar effective temperature, metallicity, surface gravity and microturbulent velocity of host stars. The stellar parameters mentioned above were based on the results of Enoch et al. (2011) and ?, and we adopted a circular orbit ($e = 0$) in following analysis of both of targets, as both Enoch et al. (2011) and ? did not find a significant non-zero eccentricity through fitting their RV curves. The Metropolis-Hastings algorithm was used to obtain the posterior probability distribution of the system parameters and the best-fit system parameters with uncertainties.

At the beginning of the analysis, we modeled all of the light curves and the RV curves simultaneously to derive the initial global system parameters of the planetary systems. The 12 RV measurements of WASP-35 were made by Enoch et al. (2011) between 2010 January 5 and 2010 February 14, and the RV curves of HAT-P-30 were observed by Enoch et al. (2011) and ? between 2010 April 27 and 2011 January 4, including 39 data points. The inputs parameters were described above, we adopted a circular orbit ($e = 0$) and other system parameters as free ones varied with the MCMC calculations. We employed 5 chains of 17,000 MCMC steps, in which 2,000 steps were burn-in samples and had been eliminated in the statistics of posterior probability distribution. This chain length was carefully considered, which had balanced convergence of the solution and computation time (Wang et al. 2013).

Then we fitted the separately to derive the mid-transit times for the TTV analysis and refining the ephemerides, using the above results as the input parameters. Other configurations followed the same procedure as above, except that the orbital periods were fixed as the input ones. The results of the mid-transit times of the targets are listed in Table 1 and Table 2, combined with several mid-transit times from previous works and the ETD website. We used a linear ephemeris formula $T = T_0 \times E$ to fit the new mid-transit times and derived the orbital period values respectively, where T_0 is the zero point of the epoch of mid-transit, P is the orbital period and E is the the cycle

Table 1. The mid-transit times of WASP-35.

Mid-time ($\text{BJD}_{\text{TDB}} - 2450000$)	Error (days)	Cycle number	Source
5531.4790700	0.0001500	0	Enoch et al. (2011)
8440.1231974	0.0002673	920	TESS
8443.2834342	0.0003904	921	YO-1m
8443.2845042	0.0002821	921	TESS
8446.4460079	0.0002735	922	TESS
8449.6077501	0.0003029	923	TESS
8452.7689812	0.0002756	924	TESS
8455.9305639	0.0002782	925	TESS
8459.0921595	0.0002948	926	TESS
8462.2537745	0.0003173	927	TESS
9157.8000120	0.0008600	1147	ETD
9176.7683243	0.0003100	1153	TESS
9176.7697320	0.0007200	1153	ETD
9179.9301275	0.0002882	1154	TESS
9183.0917244	0.0003045	1155	TESS
9189.4143000	0.0003028	1157	TESS
9192.5756463	0.0003310	1158	TESS
9195.7378575	0.0003504	1159	TESS
9195.7389020	0.0006300	1159	ETD
9198.8988431	0.0003170	1160	TESS
9252.6467690	0.0009600	1177	ETD
9524.5411270	0.0006800	1263	ETD

number. we preformed the MCMC calculations to find the best-fitting linear ephemeris formula by using the **emcee** package (Foreman-Mackey et al. 2013). We ran 50,000 MCMC steps with 1,000 burn-in steps to ensure convergence and the final results are $T(\text{BJD}_{\text{TDB}} - 2450000) = 5531.47909(15) + 3.1615692(2) \times E$ for the WASP-35 system and $T(\text{BJD}_{\text{TDB}} - 2450000) = 5523.92157(48) + 2.8106006(4) \times E$ for the HAT-P-30 system.

Using the new orbital periods derived above as the input parameters and keeping fixed, the final system parameters of the targets were calculated based on all the light curves and the RV curves following the same strategy as above. The final solutions of the system parameters for WASP-35 and HAT-P-30 systems are listed in Table 3 and Table 4 together with the results of Enoch et al. (2011) and ? for comparison. The final transit modeling results are shown in Figure 5 and Figure 6.

5. TTV MODELING AND PROSPECT ON ATMOSPHERIC PROPERTIES

5.1. TTV signals

Transit timing variations are generally parameterized with the deviations between the observed transit times and their expected values assuming a Keplerian motion for the planet. The TTVs for these two targets were computed based on our new observations, TESS photometry, transit observations collected from ETD as well as transit observations in the literature. In tables 1 and 2, there exist discrepancies between the transit times derived from simultaneous TESS and ground-based observations for some transit events, which may mean that the timing uncertainties were slightly underestimated, especially for the ground-based transit light curves which have lower quality than the TESS ones. Thus, we added a timing jitter to cope with this issue in the following TTV modeling. Refined orbital periods were obtained by linearly fitting all available transit times, in terms of a total of 55 transit times of HAT-P-30b, and 22 of WASP-35b. Figure 7 presents all the TTV measurements for transiting exoplanet WASP-35b, and Figure 8 for HAT-P-30b.

As the degeneracy in the explanation for hot Jupiter’s TTVs mentioned in Section 1, we used four different models, namely linear ephemeris model, orbital decay model, the elliptical orbit precession model, and planetary interaction-

Table 2. The mid-transit times of HAT-P-30.

Mid-time (BJD _{TDB} - 2450000)	Error (days)	Cycle number	Source
5290.6368010	0.0043224	-83	?
5523.9198071	0.0003303	0	?
5650.3954100	0.0030500	45	ETD
5928.6491100	0.0009000	144	ETD
5945.5120500	$^{+0.0005400}_{-0.0004900}$	150	Maciejewski et al. (2016)
5945.5136000	0.0019300	150	ETD
5970.8068390	0.0016200	159	ETD
5976.4282790	0.0012500	161	ETD
5976.4288790	0.0011800	161	ETD
6240.6257120	0.0012300	255	ETD
6296.8385100	0.0011600	275	ETD
6679.0801200	0.0013400	411	Wang et al. (2021)
6704.3729040	0.0011600	420	ETD
7449.1875100	0.0018300	685	Wang et al. (2021)
7460.4253570	0.0011000	689	ETD
7775.2132600	0.0008300	801	Wang et al. (2021)
8140.5896250	0.0013300	931	ETD
8143.4050250	0.0012000	932	ETD
8157.4556750	0.0013400	937	ETD
8171.5092660	0.0015600	942	ETD
8441.3230170	0.0007651	1038	YO-1m
8491.9157947	0.0004482	1056	TESS
8494.7259289	0.0005524	1057	TESS
8497.5365477	0.0004330	1058	TESS
8500.3478024	0.0004888	1059	TESS
8505.9685566	0.0004930	1061	TESS
8508.7796351	0.0004426	1062	TESS
8511.5901344	0.0004888	1063	TESS
8514.3994518	0.0004482	1064	TESS
8528.4546490	0.0009200	1069	ETD
8528.4557390	0.0009200	1069	ETD
8573.4253810	0.0009200	1085	ETD
8806.7005660	0.0011600	1168	ETD
8882.5887080	0.0011400	1195	ETD
8882.5893000	0.0009000	1195	Edwards et al. (2021)
8885.4015610	$^{+0.0015510}_{-0.0014810}$	1196	Saha et al. (2021)
8885.4011690	$^{+0.0006960}_{-0.0007720}$	1196	Saha et al. (2021)
8902.2651870	$^{+0.0008220}_{-0.0009760}$	1202	Saha et al. (2021)
8919.1281410	$^{+0.0020980}_{-0.0016200}$	1208	Saha et al. (2021)
8933.1758110	$^{+0.0017660}_{-0.0017940}$	1213	Saha et al. (2021)
8944.4227790	0.0006700	1217	ETD
9191.7550600	0.0009700	1305	ETD
9194.5669500	0.0016300	1306	ETD
9231.1039217	0.0005250	1319	TESS
9233.9144487	0.0004940	1320	TESS
9236.7243179	0.0005188	1321	TESS
9236.7251900	0.0014100	1321	ETD
9239.5357656	0.0004714	1322	TESS
9245.1565895	0.0004347	1324	TESS
9247.9672925	0.0004558	1325	TESS

Table 2. Continued.

Mid-time (BJD _{TDB} - 2450000)	Error (days)	Cycle number	Source
9250.7776903	0.0004371	1326	TESS
9250.7751800	0.0012100	1326	ETD
9253.5871352	0.0006276	1327	TESS
9253.5907500	0.0008000	1327	ETD
9256.3947700	0.0012000	1328	ETD

Table 3. System parameters of WASP-35.

Parameter	Enoch et al. (2011)	This work
Orbital period (days)	3.161575±0.000002	3.1615691±0.0000003
Transit epoch (BJD-2450000)	5531.47984±0.00015	5531.47920±0.00029
Transit Duration (days)	0.1278±0.0009	0.1304±0.0004
Planet/star area ratio	0.0154±0.0002	0.0153±0.0001
Impact parameter	0.30 ^{+0.06} _{-0.09}	0.299±0.003
Stellar reflex velocity (m/s)	94.82 ^{+7.11} _{-7.18}	98.90±3.64
Centre-of-mass velocity (km/s)	17.718±0.004	17.7284±0.0003
Orbital separation (AU)	0.04317±0.00033	0.04360±0.00020
Orbital inclination (deg)	87.96 ^{+0.62} _{-0.49}	87.95±0.33
Orbital eccentricity	0 (fixed)	0 (fixed)
Stellar mass (M_{\odot})	1.07±0.03	1.106±0.015
Stellar radius (R_{\odot})	1.09±0.03	1.122±0.016
Stellar density (ρ_{\odot})	0.83±0.07	0.784±0.031
Stellar surface gravity (cgs)	4.40±0.02	4.381±0.011
Stellar metallicity	-0.15±0.09	-0.051±0.051
Stellar effective temperature (K)	5990±90	6072±63
Planet mass (M_{Jup})	0.72±0.06	0.765±0.029
Planet radius (R_{Jup})	1.32±0.05	1.349±0.022
Planet density (ρ_{Jup})	0.32±0.04	0.311±0.019
Planet surface gravity (log g_{Jup})	2.98±0.04	2.983±0.021
Planet effective temperature ($A=0$) (K)	1450±30	1484±18

induced TTV model, to fit the timing data of HAT-P-30b and WASP-35b. In this section we describe our analyses on the first three models, while the last one will be presented in Section 5.2. Our timing analysis was partly similar to Patra et al. (2017), Yee et al. (2020) and Turner et al. (2021).

The first model assumes a constant period:

$$T_{tra}(E) = T_0 + P \times E$$

where T_0 is the reference mid-transit time and E is the cycle number.

The second model assumes the planet has a constant orbital period decay rate:

$$T_{tra}(E) = T_0 + P \times E + \frac{1}{2} \frac{dP}{dE} E^2$$

where dP/dE is the decay rate.

The third model assumes the planet has a nonzero orbital eccentricity e and the argument of pericenter ω is precessing uniformly over time:

$$T_{tra}(E) = T_0 + P_s \times E - \frac{eP_a}{\pi} \cos\omega(E)$$

Table 4. System parameters of HAT-P-30.

Parameter	?	Enoch et al. (2011)	This work
Orbital period (days)	2.810595±0.000005	2.810603±0.000008	2.8106006±0.0000004
Transit epoch (BJD-2450000)	5456.46561±0.00037	5571.70135±0.00016	5523.92157±0.00043
Transit Duration (days)	0.0887±0.0015	0.0920±0.0008	0.0916±0.0004
Planet/star area ratio	0.0128±0.0004	0.0122±0.0002	0.0124±0.0001
Impact parameter	0.854 ^{+0.008} _{-0.010}	0.87±0.01	0.872±0.003
Stellar reflex velocity (m/s)	92.67±2.50	97.70 ^{+6.19} _{-6.40}	92.67±2.50
Centre-of-mass velocity (km/s)	45.51±0.18	44.677±0.001	44.6708±0.0002
Orbital separation (AU)	0.0419±0.0005	0.04118±0.00031	0.04114±0.00030
Orbital inclination (deg)	83.6±0.4	82.48 ^{+0.16} _{-0.15}	82.56±0.08
Orbital eccentricity	0.035±0.024	0 (fixed)	0 (fixed)
Stellar mass (M_{\odot})	1.242±0.041	1.18±0.03	1.175±0.025
Stellar radius (R_{\odot})	1.215±0.051	1.33±0.03	1.314±0.015
Stellar density (ρ_{\odot})		0.50±0.02	0.517±0.012
Stellar surface gravity (cgs)	4.36±0.03	4.26±0.01	4.270±0.007
Stellar metallicity	+0.13±0.08	-0.08±0.08	-0.079±0.079
Stellar effective temperature (K)	6304±88	6250±100	6252±100
Planet mass (M_{Jup})	0.711±0.028	0.76±0.05	0.723±0.023
Planet radius (R_{Jup})	1.340±0.065	1.42±0.03	1.426±0.020
Planet density (ρ_{Jup})	0.28±0.04	0.26±0.03	0.249±0.011
Planet surface gravity (log g_{Jup})	2.99±0.04	2.93±0.03	2.910±0.015
Planet effective temperature ($A=0$) (K)	1630±42	1710±30	1704±28

$$\omega(E) = \omega_0 + \frac{d\omega}{dE}E$$

$$P_s = P_a \left(1 - \frac{1}{2\pi} \frac{d\omega}{dE} \right)$$

where P_s is the sidereal period, P_a is the anomalistic period and $d\omega/dE$ is the precession rate (Giménez & Bastero 1995).

For the these models, we preformed the MCMC calculations to find the best-fitting parameters using the **emcee** package (Foreman-Mackey et al. 2013) and ran 50,000 MCMC steps with 1,000 burn-in steps to ensure convergence. The results of three timing model fitting are listed in Table 5 and Table 6, and Figure 7 and Figure 8 show the transit timing data with the best-fitting orbital decay and apsidal precession models.

We used the Bayesian Information Criterion (BIC; Schwarz 1978) as the penalty to compare two different best-fit models, and the BIC is defined as:

$$\text{BIC} = \chi^2 + k \log n$$

where k is the number of free parameters and n is the number of data points.

5.1.1. WASP-35

Figure 7 is the linear plot of TTV versus cycle for this planet. The deviations of the transit times from the linear ephemeris have a RMS of 37 s. Compared with the constant period model ($\chi_{min}^2 = 22.807$) and the apsidal precession model ($\chi_{min}^2 = 22.254$), the orbital decay model had a lower minimum chi-squared ($\chi_{min}^2 = 22.168$). But we found that the constant period model had the lowest BIC value, that is, the constant period model was the favored model with $\Delta(\text{BIC}_{1,2}) = 2.452$ and $\Delta(\text{BIC}_{1,3}) = 8.720$. We assumed a multivariate Gaussian distribution for the posterior of all the parameters, the Bayes factor B :

$$B_{1,2} = \text{EXP}[-\Delta(\text{BIC})/2] = 3.408$$

$$B_{1,3} = \text{EXP}[-\Delta(\text{BIC})/2] = 78.257$$

This means that the observations of WASP-35 slightly favored the constant period model.

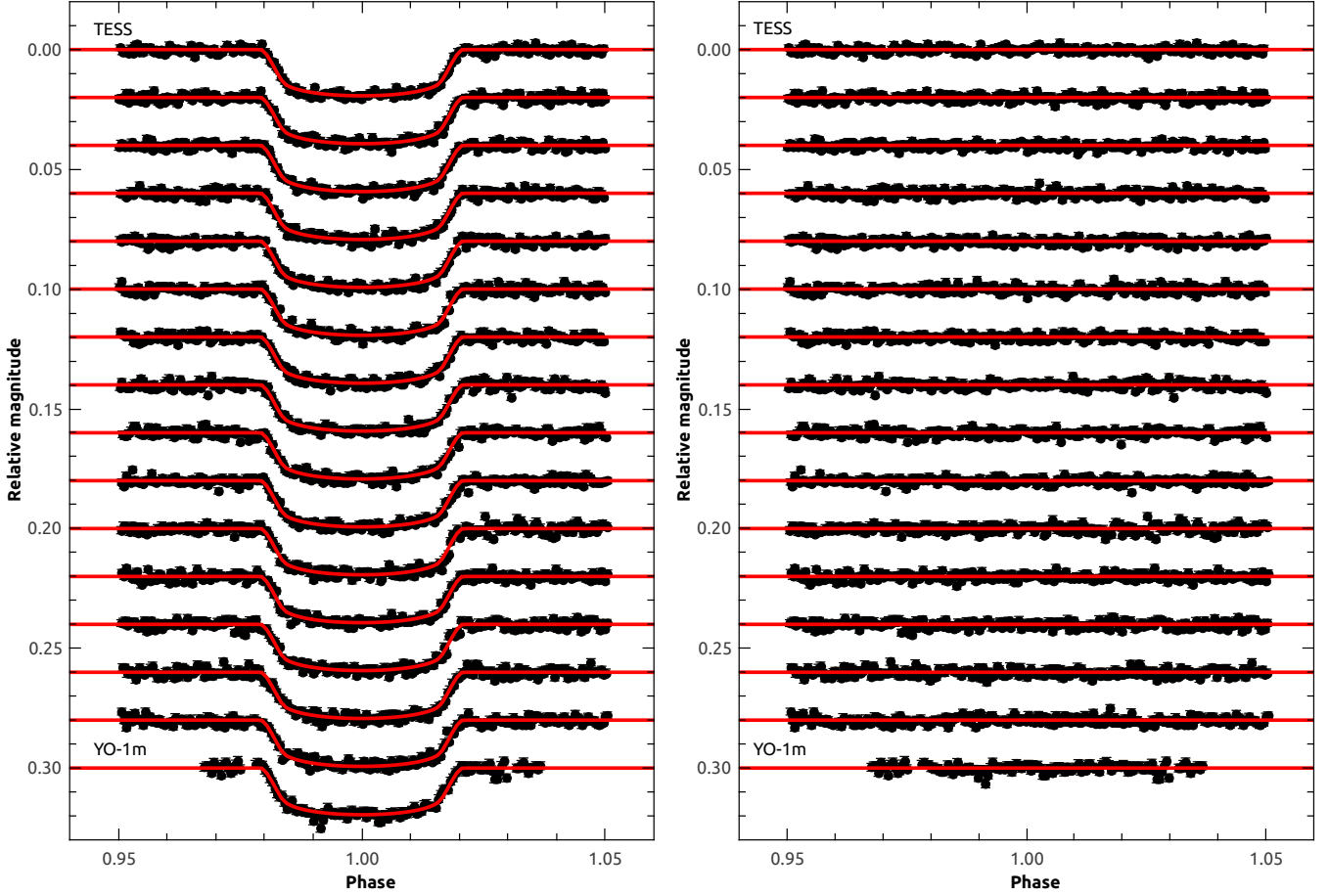


Figure 5. The final transit light curves of WASP-35 with the best-fitting transit models and the residuals.

5.1.2. HAT-P-30

Figure 8 is the linear plot of TTV versus cycle for this planet. Compared with the TTV analysis of Kokori et al. (2021), our data set covers a longer time baseline and contains more data points, which exhibits a secular timing effect of HAT-P-30b. The deviations of the transit times from the linear ephemeris have a RMS of 158 s. Compared with the constant period model ($\chi_{min}^2 = 119.220$) and the orbital decay model ($\chi_{min}^2 = 113.793$), the apsidal precession model had a lower minimum chi-squared ($\chi_{min}^2 = 100.051$). And we also found that the apsidal precession model had the lowest BIC value, that is, the apsidal precession model was the favored model with $\Delta(\text{BIC}_{3,1}) = 19.744$ and $\Delta(\text{BIC}_{3,2}) = 9.095$. We assumed a multivariate Gaussian distribution for the posterior of all the parameters, the Bayes factor B :

$$B_{3,1} = \text{EXP}[-\Delta(\text{BIC})/2] = 35.641$$

$$B_{3,2} = \text{EXP}[-\Delta(\text{BIC})/2] = 17.523$$

This means slightly favored to the apsidal precession model for the observations.

According to the constant-phase lag model for tidal evolution suggested by Goldreich & Soter (1966), the decay rate is defined as:

$$\frac{dP}{dt} = -\frac{27\pi}{2Q'_*} \left(\frac{M_p}{M_*}\right) \left(\frac{R_*}{a}\right)$$

where Q'_* is the modified quality factor of the stellar tidal oscillations, M_p is the planet mass, M_* is the stellar mass. For the HAT-P-30, this yields

$$\frac{dP}{dt} = -553.08 \pm 245.52 \text{ ms yr}^{-1}$$

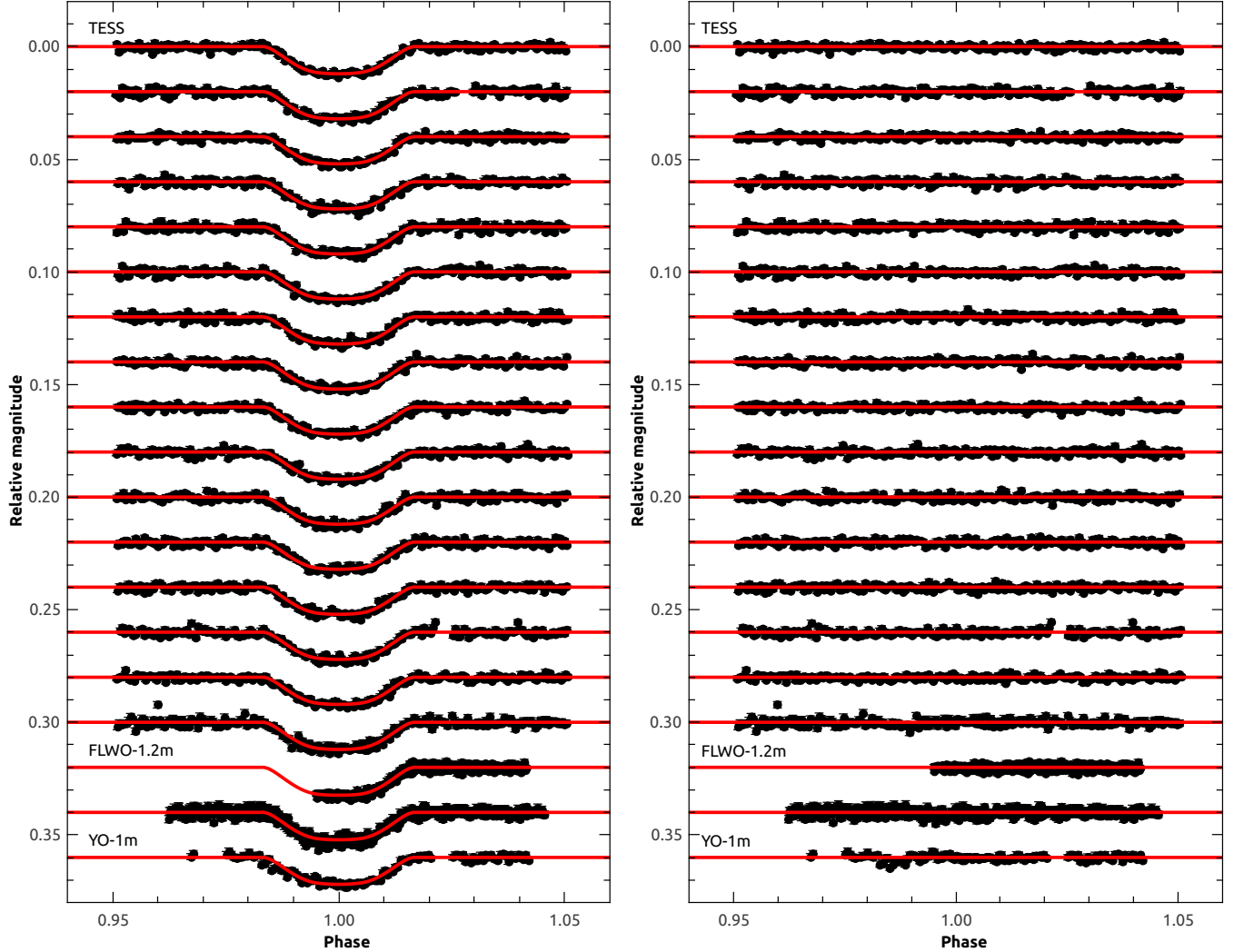


Figure 6. The final transit light curves of HAT-P-30 with the best-fitting transit models and the residuals.

Based on the decay rate of the orbital decay model, we derived the modified quality factor of

$$Q'_* = (8.10 \pm 3.62) \times 10^2$$

This value is significantly lower compared with the typical values of $10^5 - 10^7$ for binary star systems (Meibom & Mathieu 2005; Meibom et al. 2015) and $10^5 - 10^{6.5}$ for hot Jupiters (Jackson et al. 2008; Husnoo et al. 2012; Barker 2020).

In addition, we also considered whether this TTV is caused by the Rømer effect like WASP-4 system as (Bouma et al. 2019, 2020). Because of the Doppler effect, if there is any line-of-sight acceleration of the system, it would lead to a decay of the orbital period:

$$\frac{dP}{dt} = \frac{\dot{v}_r P}{c}$$

where \dot{v}_r represents the line-of-sight acceleration of the radial motion. We performed an independent RV modeling to test this possibility. We modeled all of the RV measurements simultaneously and other configurations followed the same procedure as above, except for a long-term linear trend \dot{v}_r . Compared with the RV model with a long-term linear trend ($\chi^2_2 = 46.291$, $\text{BIC}_2 = 52.610$, see Figure 9), the RV model without a long-term linear trend has a lower χ^2 ($\chi^2_1 = 46.260$) and BIC value ($\text{BIC}_1 = 50.999$), namely the best-fitting result prefers the RV model without a long-term linear trend. We assumed a multivariate Gaussian distribution for the posterior of all the parameters, the

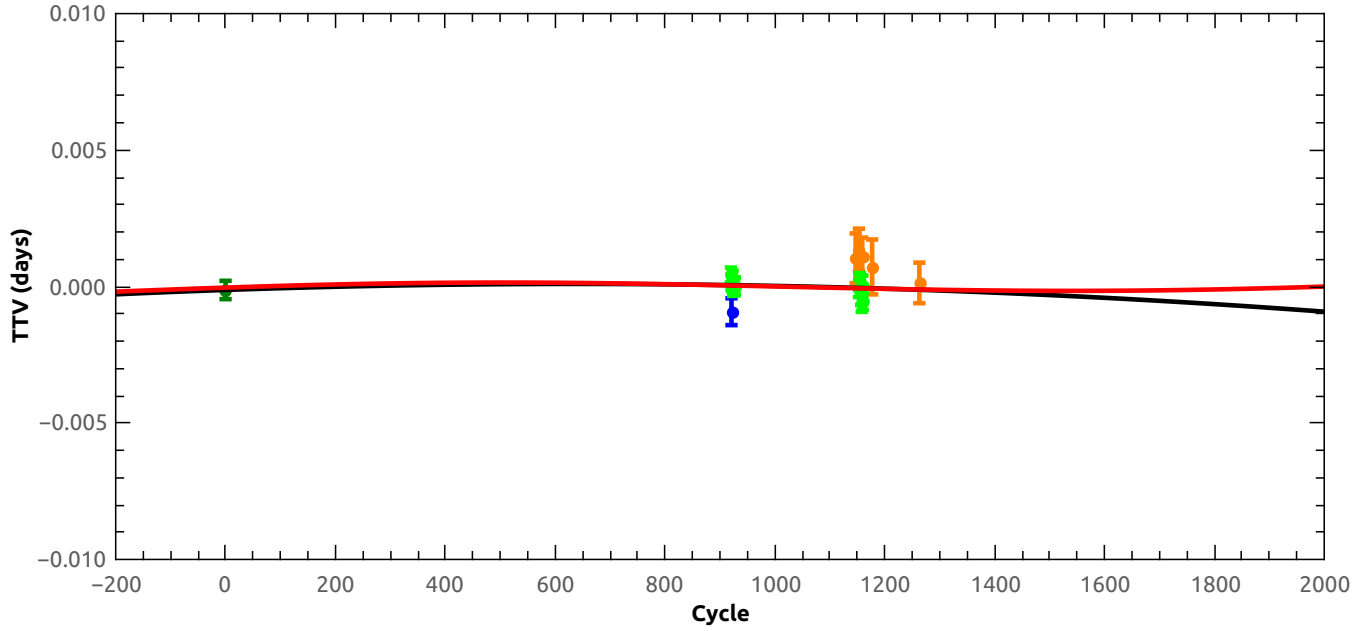


Figure 7. Transit timing variations after subtracting the constant-period model of WASP-35. The green and blue dots are the new transit times from TESS and YO-1m, the olive ones are from [Enoch et al. \(2011\)](#), and the orange ones denote those data points from ETD. The black curve shows the expected orbital decay model and the red curve shows the apsidal precession model.

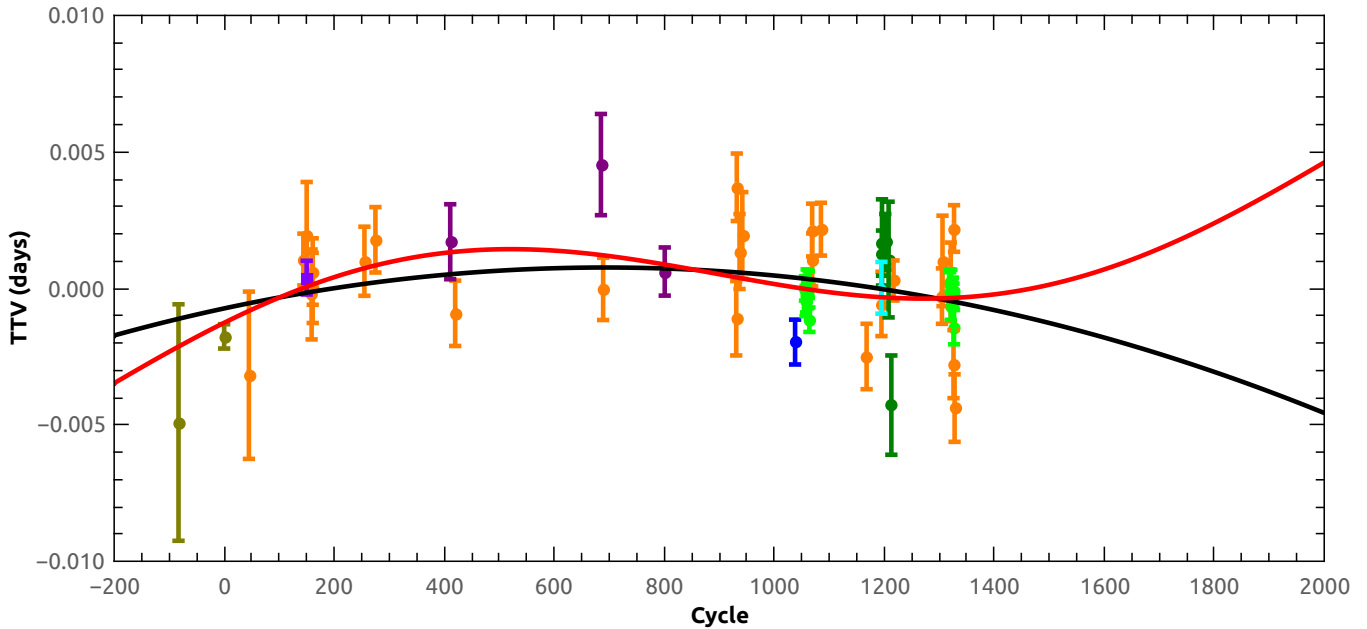


Figure 8. Transit timing variations after subtracting the constant-period model of HAT-P-30. The green and blue dots are the new transit times from TESS and YO-1m, the dark yellow ones are refined transit times from the data of [?](#), the violet one is from the data of [Maciejewski et al. \(2016\)](#), the purple ones are from [Wang et al. \(2021\)](#), the olive ones are from [Saha et al. \(2021\)](#), the cyan one is from [Edwards et al. \(2021\)](#) and the orange ones denote those from ETD. The black curve shows the expected orbital decay model and the red curve shows the apsidal precession model.

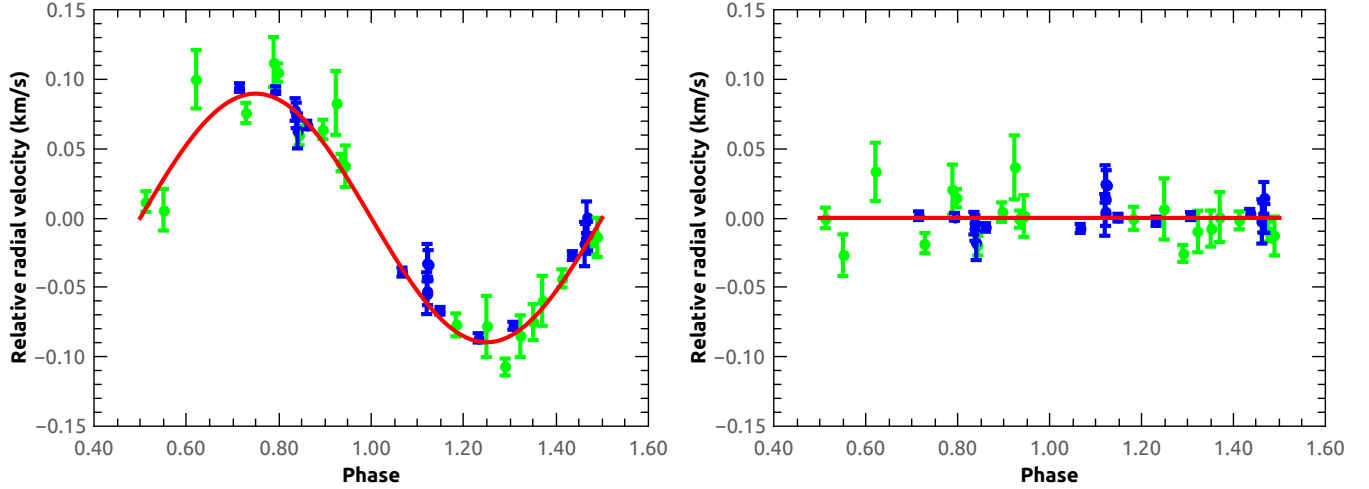


Figure 9. The RV data of HAT-P-30 with the linear trend best-fitting model and the residuals (right panel). The green dots are the RV data from [Enoch et al. \(2011\)](#) and the blue ones are from ?.

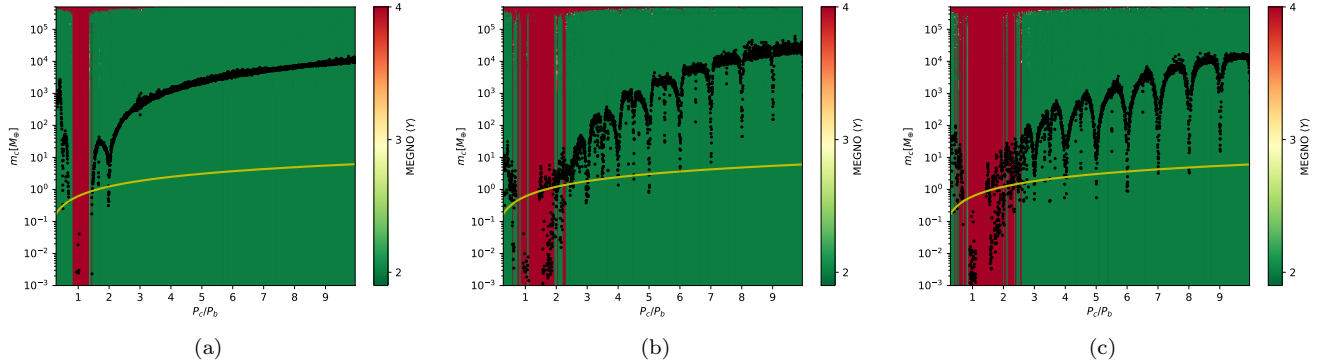


Figure 10. The MEGNO maps of WASP-35 with the perturber initially on coplanar + circular orbit (a), coplanar+slightly eccentric orbit ($e = 0.2$) (b), inclined+slightly eccentric orbit ($e = 0.2$) (c), respectively. The dark dots represent the upper mass limit of the RMS of WASP-35b's TTVs, while the yellow curves are from the constraints of RMS of WASP-35's RV residuals after removing the components of WASP-35b. The regular orbital configurations denoted with green are distinguished from the chaotic ones labeled with red on the MEGNO map.

Bayes factor B :

$$B_{1,2} = \text{EXP}[-\Delta(\text{BIC})/2] = 2.237$$

This means the difference between two RV models is not more than a bare mention.

We preformed the MCMC calculations to derive the value of line-of-sight acceleration \dot{v}_r . The configurations of MCMC calculations are as above, and the value of line-of-sight acceleration

$$\dot{v}_r = -0.013 \pm 0.017 \text{ m s}^{-1} \text{ day}^{-1}$$

For the HAT-P-30, this yields

$$\frac{dP}{dt} = -3.85 \pm 5.03 \text{ ms yr}^{-1}$$

Based on the line-of-sight acceleration we obtained, the implied period derivative is about two orders of magnitude smaller than the decay rate observed from transit timing, so the $R\dot{\theta}$ effect cannot account for all of the observed period decrease.

5.2. Upper Mass Limit of a Hypothetical Perturber

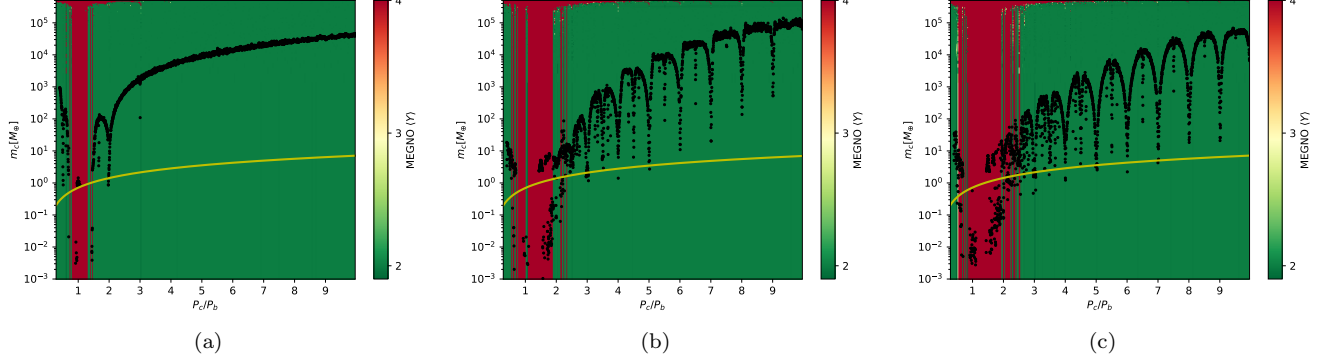


Figure 11. The MEGNO maps of HAT-P-30 with the perturber initially on coplanar + circular orbit (a), coplanar+slightly eccentric orbit ($e = 0.2$) (b), inclined+slightly eccentric orbit ($e = 0.2$) (c), respectively. The dark dots represent the upper mass limit of the RMS of HAT-P-30b’s TTVs, while the yellow curves are from the constraints of RMS of HAT-P-30’s RV residuals after removing the components of HAT-P-30b. The regular orbital configurations denoted with green are distinguished from the chaotic ones labeled with red on the MEGNO map.

Table 5. Timing model parameters of WASP-35.

Parameter	Symbol	Unit	Value
Constant period model			
Period	P	days	3.1615691 ± 0.0000003
Mid-transit time	T_0	BJD _{TDB}	$2455531.47920 \pm 0.00029$
N_{dof}			20
χ^2_{min}			22.807
BIC			28.989
Orbital decay model			
Period	P	days	3.1615698 ± 0.0000009
Mid-transit time	T_0	BJD _{TDB}	$2455531.47907 \pm 0.00033$
Decay rate	dP/dE	days/orbit	$-1.09 \times 10^{-9} \pm 1.36 \times 10^{-9}$
N_{dof}			19
χ^2_{min}			22.168
BIC			31.441
Apsidal precession model			
Sidereal period	P_s	days	3.1615693 ± 0.0000004
Mid-transit time	T_0	BJD _{TDB}	$2455531.47902 \pm 0.00033$
Orbital eccentricity	e		0.00024 ± 0.00017
Argument of periastron	ω_0	rad	2.145 ± 0.540
Precession rate	$d\omega/dE$	rad/orbit	0.00244 ± 0.00170
N_{dof}			17
χ^2_{min}			22.254
BIC			37.709

The results from our TTV measurements (see Section 5.1) allow to infer the upper mass limit for an additional perturbing planet in each of these two systems, which assuming that all the TTV signals origin from the gravitational interactions among planets involved. Although inverting the high-cadence and high signal-to-noise TTV signals could be used to measure the mass and eccentricity of the perturbing exoplanets, obviously that is not our cases for HAT-P-30b and WASP-35b. However, the perturbation from the additional planet can be approximately quantified by the RMS of TTVs for our sparse measurements. The TTV effects are strongly amplified for orbital configurations in

Table 6. Timing model parameters of HAT-P-30.

Parameter	Symbol	Unit	Value
Constant period model			
Period	P	days	2.8106006 ± 0.0000004
Mid-transit time	T_0	BJD _{TDB}	$2455523.92157 \pm 0.00043$
N_{dof}			53
χ^2_{min}			119.220
BIC			127.235
Orbital decay model			
Period	P	days	2.8106049 ± 0.0000019
Mid-transit time	T_0	BJD _{TDB}	$2455523.92083 \pm 0.00047$
Decay rate	dP/dE	days/orbit	$-6.24 \times 10^{-9} \pm 2.77 \times 10^{-9}$
N_{dof}			52
χ^2_{min}			113.793
BIC			125.815
Apsidal precession model			
Sidereal period	P_s	days	2.8106047 ± 0.0000011
Mid-transit time	T_0	BJD _{TDB}	$2455523.91840 \pm 0.00090$
Orbital eccentricity	e		0.00323 ± 0.00065
Argument of periastron	ω_0	rad	2.290 ± 0.325
Precession rate	$d\omega/dE$	rad/orbit	0.00270 ± 0.00050
N_{dof}			50
χ^2_{min}			100.051
BIC			120.088

(or near) Mean-Motion Resonances (MMR) (Agol et al. 2005; Holman & Murray 2005), in which the detection of a low-mass planetary perturbing body will in principle be permitted.

An upper mass limit can be obtained by employing a N -body code to perform direct orbit integrations, which is widely used in the literature (e.g., Wang et al. 2017, 2018a,b, 2021; Cortés-Zuleta et al. 2020). Within the framework of the three-body orbital configuration, we numerically integrated the orbits of each of these two hot Jupiters and a hypothetical perturbing planet around their host star. To meet our need, we modified the TTV inversion code of Sun et al. (2019), which employs **TTVFast** (Deck et al. 2014) to perform direct orbit integrations. Summarily, our new code calculates the RMS of synthetic TTVs, whose epochs are selected to be identical to those of measured TTVs, considering a transiting exoplanet perturbed by an $1M_{\oplus}$ planet on an arbitrary orbital architecture. Such a configuration will help simplify the computing of upper mass limit, as the amplitude of a TTV pattern is linearly proportion to the mass of perturbing planet. Hence, the upper mass limit of perturbing planet could be well estimated by the product of the RMS of measured TTVs divided by that of synthetic TTVs.

This code was then applied to a series of orbital periods of the perturbing planet while fixing all the other orbital parameters. As the TTV patterns strongly depended on the perturber’s mass, the orbital period, the eccentricity, and the mutual inclination of the orbit (Agol et al. 2005; Holman & Murray 2005; Nesvorný & Morbidelli 2008; Lithwick et al. 2012; Xie et al. 2014), we performed orbital integrations in terms of three different orbital architectures for hypothetical perturbers in this study: (a) initially on coplanar and circular orbit; (b) initially on coplanar and slightly eccentric orbit (i.e., $e_c = 0.2$); (c) initially on inclined and slightly eccentric orbit (i.e., $i_c = i_b - 30^\circ$, $e_c = 0.2$, where i_b and i_c denote the inclinations of the known transiting planet and the perturber, respectively). For clarity, hereafter we label these three different orbital architectures as Case a, Case b, and Case c, respectively. Except the orbital period of the perturbing planet, the remaining orbital elements (i.e., the longitude of the ascending node Ω , the argument of periastron ω , and the mean anomaly M at a reference time) were fixed to selected values, $\Omega_c = \Omega_b = 0$, $\omega_c = \omega_b = 90^\circ$, $M_c = M_b + 180^\circ$; the orbital period of the hypothetical perturber P_c was searched from 1 day to $10P_b$ with a step of 0.007 days. We expect that the first setting would provide a most conservative estimate of the upper mass limit of a possible perturber (Bean 2009; Fukui et al. 2011; Hoyer et al. 2011, 2012; Cortés-Zuleta et al. 2020).

In addition, the RVs of the host star induced by a hypothetical perturber could place constraints on the perturber’s mass. If the planets are on non-interacting Keplerian orbits, the RVs of the host star are the sum of the RVs arose by each planetary component’s Keplerian motion (Ford 2006). Therefore, the residuals of both HAT-P-30 and WASP-35’s RVs after removing the contributions from both known planets could well present the RVs induced by additional bodies. Placing good constraints on the mass of the additional body through fitting RV curves requires a good coverage in its orbit phase and high signal-to-noise RV measurements, however, which is not the cases for the hypothetical perturbers in both HAT-P-30 and WASP-35. Therefore, we used the RMS of the residuals of both HAT-P-30 and WASP-35’s RVs instead of the residuals to statistically constrain the mass of the hypothetical perturber. The amplitude of RV curves K arose by a planet on its host star is scaled with the following formula:

$$\left(\frac{M_p \sin i_p}{M_\oplus}\right) = 11.19 \left(\frac{K}{m/s}\right) \sqrt{1-e^2} \left(\frac{M_*}{M_\odot}\right)^{2/3} \left(\frac{P_{orb}}{1yr}\right)^{1/3}$$

where M_p , M_* , and P_{orb} are the mass of the planet, the mass of the host star, and the orbital period of the planet, respectively. For the orbital eccentricities (i.e., $e_c \leq 0.2$) of the perturbers we assumed, the RMS of RV curves statistically equals about $\sqrt{2}/2$ times of the RV amplitude. We obtained the mass limits, that is, the yellow curves in Figure 10 and Figure 11 of the hypothetical perturbers based on the RMS of both HAT-P-30 and WASP-35’s RV residuals derived in Section 4.

Some constraints could also be placed on the perturber’s mass by the requirements of the long-term stability of perturber’s orbits. For this purpose, we computed the Mean Exponential Growth factor of Nearby Orbits (MEGNO; Cincotta & Simó 2000; Goździewski et al. 2001; Cincotta et al. 2003), which was originally developed to study the global dynamics of non-axisymmetric galactic potentials, by employing **REBOUND** to perform direct orbital integrations and calculate associated variational equations of motion over a grid of initial values of orbital parameters (Rein & Liu 2012; Rein & Tamayo 2015, 2016). In addition to the orbital period of the perturber, here we also adjusted its mass; we integrated each initial grid point for 500 years (i.e., $\sim 10^4$ of orbital periods of transiting exoplanets), which will highlight the location of weak chaotic high-order mean-motion resonances. MEGNO is often used to quantitatively measure the degree of stochastic behaviour of a non-linear dynamical system and thus detect the chaotic resonances (Goździewski et al. 2001; Hinse et al. 2010). In addition to integrating the Newtonian equations of motion, the associated variational equations of motion are calculated simultaneously for obtaining the MEGNO at each integration time step. Following Cincotta & Simó (2000) and Cincotta et al. (2003), the MEGNO index is defined as:

$$Y(t) = \frac{2}{T} \int_0^T \frac{\|\dot{\delta}(t)\|}{\|\delta(t)\|} t dt$$

where $\dot{\delta}/\delta$ is the relative change of the variational vector δ . The time-averaged or mean $Y(t)$ is parameterized with:

$$\langle Y(t) \rangle = \frac{1}{T} \int_0^T Y(t) dt$$

For the results in Figure 10 and Figure 11, it is always the time-averaged MEGNO index that is utilized to quantitatively differentiate between quasi-periodic and chaotic dynamics. The regular orbits which evolve quasi-periodically in time $\langle Y \rangle$, will asymptotically approach 2.0 for $t \rightarrow \infty$, while for chaotic orbits it grows, proportionally to the Lyapunov exponent Λ , as $(\Lambda/2)T$. For a chaotic orbital evolution $\langle Y \rangle$ significantly deviates from 2.0 with orbital parameters exhibiting erratic temporal evolutions. Importantly, MEGNO is unable to prove whether a dynamical system is evolving quasi-periodically. This hints that a given system cannot be proven to be stable or bounded for all times. For a given initial condition once MEGNO detected chaotic behaviors, however, there is no doubt about its erratic nature in the future (Hinse et al. 2010).

In the following parts, we present the results of each system for which we have calculated the RMS scatter of TTVs (TTV_{RMS}) on a series of orbital periods of a perturbing planet. In each of the three cases, we found the common instability regions located in the proximity of the transiting planet with MEGNO color-coded as yellow (corresponding to $\langle Y \rangle > 3.5$).

5.2.1. WASP-35b

Through over-plotting the TTV_{RMS} for a certain value, we found similar results to those of Agol et al. (2005) and Holman & Murray (2005), which suggest that the TTVs are relatively more sensitive to orbital architectures

involving MMRs. Furthermore, TTV_{RMS} of both Case b and c are more complex, for which high-order MMRs (e.g., $P_c/P_b \simeq 4:1, 5:1$, and so on.) generate large TTV signals and thus the corresponding upper mass limit dramatically drops, comparing with that of Case a; interestingly, a perturbing body of only $\sim 0.606 M_{\oplus}$ located near 1:1 MMRs in Case b could well reproduce measured TTV_{RMS} of WASP-35 b. While over-plotting the RMS of RV residuals (RV_{RMS}) for a certain value with removing the component due to known WASP-35b, we found that the constraints due to RV_{RMS} on the upper mass limit are more stringent than those due to TTV_{RMS} . For HAT-P-30, similar conclusion has been drawn. As shown in Figure 10, we found that a coplanar perturbing body of mass (upper limit) around $0.606 - 1 M_{\oplus}$ initially with circular orbit will cause a RMS of 37s when located in the $P_c/P_b = 1:3$ and $2:1$. For the perturber on more inclined, and/or initially slightly eccentric orbits the high order resonances (i.e., $P_c/P_b = 4:1, 5:1$ and $6:1$ for Case b and even $P_c/P_b = 7:1$ and $8:1$ for Case c) appear beneath the upper mass limit of RV_{RMS} in addition to the co-orbital configuration (i.e., 1:1 MMR).

5.2.2. HAT-P-30b

For the HAT-P-30 system the measured TTV_{RMS} was 158s. Additional bodies in Case a with an upper mass limit as low as $\sim 0.356 M_{\oplus}$ at the 1:2 and $\sim 1.423 M_{\oplus}$ at the 2:1 MMR could cause the observed TTV scatter. Hypothetical planets of $0.712 M_{\oplus}, 1.423 M_{\oplus}, 2.135 M_{\oplus}, 2.846 M_{\oplus}$, and $3.558 M_{\oplus}$ could well produce the observed TTV_{RMS} located near 1:1, 2:1, 3:1, 4:1 and 5:1 exterior MMRs in Case b, respectively; and $2.135 M_{\oplus}, 2.491 M_{\oplus}, 2.846 M_{\oplus}, 3.558 M_{\oplus}, 4.270 M_{\oplus}$ and $4.981 M_{\oplus}$ near 3:1, 7:2, 4:1, 5:1, 6:1 and 7:1 exterior MMRs in Case c, respectively. In both Case b and c, the structure of upper mass limits is quite complex from 2:1 to 3:1 exterior MMRs, see Figure 11 for further details.

5.3. Prospect on atmospheric properties

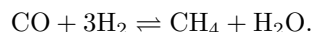
Transiting exoplanets offer the possibility of characterising the planetary atmosphere using observations at different orbital phases. These observations include the transmission spectrum during the transit (Charbonneau et al. 2002; Deming et al. 2013), the emission spectrum at secondary eclipse (Showman & Guillot 2002; Cho et al. 2003) and the phase curve throughout the orbit (Cowan & Agol 2008; Mallama 2009). The transmission spectrum probes the wavelength-dependent extinction due to the planetary atmosphere at its day–night terminator region by using photometric or spectroscopic observations (Seager & Sasselov 2000; Brown 2001; Ehrenreich et al. 2006). For hot Jupiters, they have relatively low densities, large radius and hot equilibrium temperatures, which will lead to large atmospheric scale heights, namely, the planets have significant atmospheric structures and thus are ideal targets for atmospheric studies. Both WASP-35b and HAT-P-30b belong to hot Jupiters. Therefore, based on the new system parameters, we attempt to predict the atmospheric properties of WASP-35b and HAT-P-30b.

For the transmission spectra, the amplitude of the transmission signals in a cloud-free atmosphere is proportional to the atmospheric scale height H :

$$H = \frac{k_B T_{eq}}{\mu_m g_b}$$

where k_B is Boltzmann’s constant, T_{eq} is the temperature of the planet, μ_m is the mean molecular mass and g_b is the surface gravity of the planet (Seager & Sasselov 2000; Brown 2001; Ehrenreich et al. 2006). According to de Wit & Seager (2013), hot Jupiters should be H/He-dominated atmosphere, and the mean molecular mass is approximately 2.3 amu, so the atmospheric scale height for WASP-35b is about to 550 km and 750 km for HAT-P-30b. So, both WASP-35b and HAT-P-30b should have distinct atmospheres, the spectral features in transmission spectra could have amplitude of $5-10H$ which are suitable for studying the properties of their atmospheres (Sing et al. 2013).

For hot Jupiters, the spectral features in the optical transmission spectrum are expected to have Na, K, TiO and VO. According to the dichotomy of highly irradiated, close-in giant planets proposed by Fortney et al. (2008) and the newly derived system parameters, both WASP-35b and HAT-P-30b are at the boundary between the pL and pM classes. Therefore we could expect that alkali metal absorption lines as well as TiO and VO likely appear in their high-precision transmission spectra. Madhusudhan et al. (2011) found the abundances of TiO and VO were strongly affected by the C/O ratio. In general, the upper atmospheric absorptions in the optical may lead to thermal inversions, such as the strong optical absorption of TiO and VO (Fortney et al. 2008) as well as the absorption of alkali metal at high C/O ratios (Mollière et al. 2015). H_2O , CO, CH_4 , CO_2 and H_2 are the major chemical and spectroscopic species which dominant the C/O ratio in the hot Jupiter atmosphere and the series of reactions can be summarized as



WASP-35b and HAT-P-30b have relative high temperatures ($T_{eq} > 1400\text{K}$), a simple way to estimate the C/O ratio of the atmosphere is observing the transmission spectra of H_2O and CH_4 in the near- to mid-infrared. Both of the systems have zero eccentricities, this means the planet remains at a constant distance from its host star, which avoids orbital-induced thermal response of the planetary atmospheric temperature and hence chemistry (Visscher 2012). Clouds and haze are common in the planetary atmospheres and strongly impact on observations of transmission spectra (Sing et al. 2013; Spyratos et al. 2021). Uniform global clouds can obscure the absorption features of prominent chemical species, patchy clouds can mimic high mean molecular weight atmospheres (Fortney 2005; Line & Parmentier 2016) and haze can produce a significant slope at optical passband in transmission spectra (Lecavelier Des Etangs et al. 2008). According to the theory of Lecavelier Des Etangs et al. (2008), assuming a power law for the cross section with wavelength in the form of $\sigma = \sigma_0(\lambda/\lambda_0)^\alpha$, the slope induced by Rayleigh scattering is given by

$$\frac{\mu g_b}{k_B} \frac{dR_p}{d \ln \lambda} = \alpha T_{eq}.$$

For the cloud-free atmosphere, the Rayleigh scattering is caused by H_2 and He, the expected value of α is -4. For the cloud atmosphere, the observable atmosphere would be smaller than pure gaseous atmosphere, so that the amplitude of absorption features would be small or the transmission spectra would be flatten and featureless.

6. CONCLUSIONS

Based on the new photometric data observed by TESS, the YO-1m and the published photometric and RV data from the CDS database and ETD website, we have carried out a re-analysis for the transiting exoplanetary systems WASP-35 and HAT-P-30 by using MCMC technique. The system parameters and ephemerides of WASP-35 and HAT-P-30 systems have been refined. The refined system parameters are consistent with the previous results with higher precisions. For each system, the uncertainty of the orbital period we obtained is one order of magnitude less than the previous value. Moreover, we find that HAT-P-30b's transits show significant timing variations which cannot be explained with a decaying orbit due to tidal dissipation and the Rømer effect, while both apsidal precession and an additional perturbing body could reproduce the signal. Based on the refined system parameters, both WASP-35b and HAT-P-30b are suitable for studying the properties of the planetary atmospheres by using transmission spectra.

We appreciate the referee for his/her valuable suggestions and comments, which lead to a obvious improvement to our manuscript. We acknowledge the supports from 1m telescope of Yunnan Observatories. This work is supported by National Natural Science Foundation of China through grants No. U1531121, No. 10873031, No. 11473066 and No. 12003063. We also acknowledge the science research grant from the China Manned Space Project with NO. CMS-CSST-2021-B09. This paper includes data collected by the TESS mission, which is funded by the NASA Explorer Program.

Facilities: TESS, YO-1m

Software: Juliet (Espinoza et al. 2019), batman (Kreidberg 2015), celerite (Foreman-Mackey et al. 2017), PyMultiNest (Buchner et al. 2014; Feroz et al. 2009), emcee (Foreman-Mackey et al. 2013), Lightkurve (Lightkurve Collaboration et al. 2018), TTVFast (Deck et al. 2014), REBOUND (Rein & Liu 2012)

REFERENCES

- Agol, E., Steffen, J., Sari, R., & Clarkson, W. 2005, Monthly Notices of the Royal Astronomical Society, 359, 567
- Agol, E., Dorn, C., Grimm, S. L., et al. 2021, The Planetary Science Journal, 2, 1
- Barker, A. J. 2020, Monthly Notices of the Royal Astronomical Society, 498, 2270
- Bean, J. L. 2009, Astronomy and Astrophysics, 506, 369
- Bouma, L. G., Winn, J. N., Howard, A. W., et al. 2020, The Astrophysical Journal, 893, L29
- Bouma, L. G., Winn, J. N., Baxter, C., et al. 2019, The Astronomical Journal, 157, 217
- Brown, T. M. 2001, Astrophysical Journal, 553, 1006
- Buchner, J., Georgakakis, A., Nandra, K., et al. 2014, Astronomy and Astrophysics, 564, A125

- Carter, J. A., & Winn, J. N. 2009, *The Astrophysical Journal*, 704, 51
- Charbonneau, D., Brown, T. M., Noyes, R. W., & Gilliland, R. L. 2002, *The Astrophysical Journal*, 568, 377
- Cho, J. Y. K., Menou, K., Hansen, B. M. S., & Seager, S. 2003, *The Astrophysical Journal*, 587, L117
- Cincotta, P. M., Giordano, C. M., & Simó, C. 2003, *Physica D Nonlinear Phenomena*, 182, 151
- Cincotta, P. M., & Simó, C. 2000, *Astronomy and Astrophysics Supplement Series*, 147, 205
- Claret, A. 2000, *Astronomy and Astrophysics*, 359, 289
- . 2004, *Astronomy and Astrophysics*, 428, 1001
- Collier Cameron, A., Pollacco, D., Street, R. A., et al. 2006, *Monthly Notices of the Royal Astronomical Society*, 373, 799
- Collier Cameron, A., Wilson, D. M., West, R. G., et al. 2007, *Monthly Notices of the Royal Astronomical Society*, 380, 1230
- Cortés-Zuleta, P., Rojo, P., Wang, S., et al. 2020, *Astronomy and Astrophysics*, 636, A98
- Cowan, N. B., & Agol, E. 2008, *The Astrophysical Journal*, 678, L129
- Davoudi, F., Jafarzadeh, S. J., Poro, A., et al. 2020, *New Astronomy*, 76, 101305
- de Wit, J., & Seager, S. 2013, *Science*, 342, 1473
- Deck, K. M., Agol, E., Holman, M. J., & Nesvorný, D. 2014, *The Astrophysical Journal*, 787, 132
- Delisle, J. B. 2017, *Astronomy and Astrophysics*, 605, A96
- Deming, D., Wilkins, A., McCullough, P., et al. 2013, *The Astrophysical Journal*, 774, 95
- Eastman, J., Siverd, R., & Gaudi, B. S. 2010, *Publications of the Astronomical Society of the Pacific*, 122, 935
- Edwards, B., Ho, C. S. K., Osborne, H. L. M., et al. 2021, *arXiv e-prints*, arXiv:2111.10350
- Ehrenreich, D., Tinetti, G., des Etangs, A. L., Vidal-Madjar, A., & Selsis, F. 2006, *Astronomy & Astrophysics*, 448, 379
- Enoch, B., Collier Cameron, A., Parley, N. R., & Hebb, L. 2010, *Astronomy and Astrophysics*, 516, A33
- Enoch, B., Anderson, D. R., Barros, S. C. C., et al. 2011, *The Astronomical Journal*, 142, 86
- Espinoza, N., Kossakowski, D., & Brahm, R. 2019, *Monthly Notices of the Royal Astronomical Society*, 490, 2262
- Evans, T. M., Aigrain, S., Gibson, N., et al. 2015, *Monthly Notices of the Royal Astronomical Society*, 451, 680
- Feroz, F., Hobson, M. P., & Bridges, M. 2009, *Monthly Notices of the Royal Astronomical Society*, 398, 1601
- Ford, E. B. 2006, *The Astrophysical Journal*, 642, 505
- Foreman-Mackey, D., Agol, E., Ambikasaran, S., & Angus, R. 2017, *The Astronomical Journal*, 154, 220
- Foreman-Mackey, D., Hogg, D. W., Lang, D., & Goodman, J. 2013, *Publications of the Astronomical Society of the Pacific*, 125, 306
- Fortney, J. J. 2005, *Monthly Notices of the Royal Astronomical Society*, 364, 649
- Fortney, J. J., Lodders, K., Marley, M. S., & Freedman, R. S. 2008, *The Astrophysical Journal*, 678, 1419
- Fukui, A., Narita, N., Tristram, P. J., et al. 2011, *Publications of the Astronomical Society of Japan*, 63, 287
- Gaia Collaboration, Brown, A. G. A., Vallenari, A., et al. 2021, *A&A*, 649, A1
- Gibson, N. P., Aigrain, S., Roberts, S., et al. 2012, *Monthly Notices of the Royal Astronomical Society*, 419, 2683
- Giménez, A., & Bastero, M. 1995, *Astrophysics and Space Science*, 226, 99
- Goldreich, P., & Soter, S. 1966, *Icarus*, 5, 375
- Goździewski, K., Bois, E., Maciejewski, A. J., & Kiseleva-Eggleton, L. 2001, *Astronomy and Astrophysics*, 378, 569
- Grimm, S. L., Demory, B.-O., Gillon, M., et al. 2018, *Astronomy and Astrophysics*, 613, A68
- Hinse, T. C., Christou, A. A., Alvarrellos, J. L. A., & Goździewski, K. 2010, *Monthly Notices of the Royal Astronomical Society*, 404, 837
- Holzer, T., Mazeh, T., Nachmani, G., et al. 2016, *The Astrophysical Journal Supplement Series*, 225, 9
- Holman, M. J., & Murray, N. W. 2005, *Science*, 307, 1288
- Hoyer, S., Rojo, P., & López-Morales, M. 2012, *The Astrophysical Journal*, 748, 22
- Hoyer, S., Rojo, P., López-Morales, M., et al. 2011, *The Astrophysical Journal*, 733, 53
- Hurt, S. A., Quinn, S. N., Latham, D. W., et al. 2021, *The Astronomical Journal*, 161, 157
- Husnoo, N., Pont, F., Mazeh, T., et al. 2012, *Monthly Notices of the Royal Astronomical Society*, 422, 3151
- Jackson, B., Greenberg, R., & Barnes, R. 2008, *The Astrophysical Journal*, 681, 1631
- Jenkins, J. M., Twicken, J. D., McCauliff, S., et al. 2016, in *Software and Cyberinfrastructure for Astronomy IV*, Vol. 9913, 99133E
- Kipping, D. M. 2013, *Monthly Notices of the Royal Astronomical Society*, 435, 2152
- Kokori, A., Tsiaras, A., Edwards, B., et al. 2021, *arXiv e-prints*, arXiv:2110.13863
- Kreidberg, L. 2015, *Publications of the Astronomical Society of the Pacific*, 127, 1161
- Langellier, N., Milbourne, T. W., Phillips, D. F., et al. 2021, *The Astronomical Journal*, 161, 287

- Lecavelier Des Etangs, A., Pont, F., Vidal-Madjar, A., & Sing, D. 2008, *Astronomy and Astrophysics*, 481, L83
- Lightkurve Collaboration, Cardoso, J. V. d. M., Hedges, C., et al. 2018, *Lightkurve: Kepler and TESS time series analysis in Python*, , ascl:1812.013
- Line, M. R., & Parmentier, V. 2016, *The Astrophysical Journal*, 820, 78
- Lithwick, Y., Xie, J., & Wu, Y. 2012, *The Astrophysical Journal*, 761, 122
- Maciejewski, G., Dimitrov, D., Mancini, L., et al. 2016, *Acta Astronomica*, 66, 55
- Madhusudhan, N., Mousis, O., Johnson, T. V., & Lunine, J. I. 2011, *The Astrophysical Journal*, 743, 191
- Mallama, A. 2009, *Icarus*, 204, 11
- Mandel, K., & Agol, E. 2002, *The Astrophysical Journal*, 580, L171
- Mazeh, T., Nachmani, G., Holczer, T., et al. 2013, *The Astrophysical Journal Supplement Series*, 208, 16
- Meibom, S., Barnes, S. A., Platais, I., et al. 2015, *Nature*, 517, 589
- Meibom, S., & Mathieu, R. D. 2005, *The Astrophysical Journal*, 620, 970
- Mollière, P., van Boekel, R., Dullemond, C., Henning, T., & Mordasini, C. 2015, *The Astrophysical Journal*, 813, 47
- Mordasini, C. 2018, *Planetary Population Synthesis*, 143
- Mordasini, C., Alibert, Y., & Benz, W. 2009, *Astronomy and Astrophysics*, 501, 1139
- Mortier, A., Santos, N. C., Sousa, S. G., et al. 2013, *Astronomy and Astrophysics*, 558, A106
- Mortier, A., Sousa, S. G., Adibekyan, V. Z., Brandão, I. M., & Santos, N. C. 2014, *Astronomy and Astrophysics*, 572, A95
- Murgas, F., Chen, G., Nortmann, L., Palle, E., & Nowak, G. 2020, *Astronomy and Astrophysics*, 641, A158
- Nesvorný, D., Chrenko, O., & Flock, M. 2021, arXiv e-prints, arXiv:2110.09577
- Nesvorný, D., Kipping, D. M., Buchhave, L. A., et al. 2012, *Science*, 336, 1133
- Nesvorný, D., & Morbidelli, A. 2008, *The Astrophysical Journal*, 688, 636
- Patra, K. C., Winn, J. N., Holman, M. J., et al. 2017, *Astronomical Journal*, 154, doi:ARTN 4 10.3847/1538-3881/aa6d75
- Pollacco, D., Skillen, I., Collier Cameron, A., et al. 2008, *Monthly Notices of the Royal Astronomical Society*, 385, 1576
- Rasmussen, C. E., & Williams, C. K. I. 2006, *Gaussian Processes for Machine Learning*
- Rein, H., & Liu, S. F. 2012, *Astronomy and Astrophysics*, 537, A128
- Rein, H., & Tamayo, D. 2015, *Monthly Notices of the Royal Astronomical Society*, 452, 376
- . 2016, *Monthly Notices of the Royal Astronomical Society*, 459, 2275
- Ricker, G. R., Winn, J. N., Vanderspek, R., et al. 2014, in *Space Telescopes and Instrumentation 2014: Optical, Infrared, and Millimeter Wave*, Vol. 9143, 914320
- Ricker, G. R., Winn, J. N., Vanderspek, R., et al. 2015, *Journal of Astronomical Telescopes, Instruments, and Systems*, 1, 014003
- Rowe, J. F., Bryson, S. T., Marcy, G. W., et al. 2014, *The Astrophysical Journal*, 784, 45
- Saha, S., Chakrabarty, A., & Sengupta, S. 2021, *The Astronomical Journal*, 162, 18
- Schwarz, G. 1978, *Annals of Statistics*, 6, 461
- Seager, S., & Sasselov, D. D. 2000, *Astrophysical Journal*, 537, 916
- Shan, S.-S., Yang, F., Lu, Y.-J., et al. 2021, arXiv e-prints, arXiv:2111.06678
- Showman, A. P., & Guillot, T. 2002, *Astronomy and Astrophysics*, 385, 166
- Sing, D. K., Lecavelier des Etangs, A., Fortney, J. J., et al. 2013, *Monthly Notices of the Royal Astronomical Society*, 436, 2956
- Spyratos, P., Nikolov, N., Southworth, J., et al. 2021, *Monthly Notices of the Royal Astronomical Society*, 506, 2853
- Sun, L., Ioannidis, P., Gu, S., et al. 2019, *Astronomy and Astrophysics*, 624, A15
- Sun, L., Gu, S., Wang, X., et al. 2017, *The Astronomical Journal*, 153, 28
- Sun, L., Ioannidis, P., Gu, S., et al. 2021, arXiv e-prints, arXiv:2111.09668
- Sun, L.-L., Gu, S.-H., Wang, X.-B., et al. 2015, *Research in Astronomy and Astrophysics*, 15, 117
- Tamuz, O., Mazeh, T., & Zucker, S. 2005, *Monthly Notices of the Royal Astronomical Society*, 356, 1466
- Tan, H. B., Wang, X. B., Gu, S. H., & Cameron, A. C. 2013, *Acta Astronomica Sinica*, 54, 527
- Turner, J. D., Ridden-Harper, A., & Jayawardhana, R. 2021, *Astronomical Journal*, 161, 72
- Visscher, C. 2012, *The Astrophysical Journal*, 757, 5
- Wang, S., Wang, X.-Y., Wang, Y.-H., et al. 2018a, *The Astronomical Journal*, 156, 181
- Wang, X.-B., Gu, S.-H., Collier Cameron, A., et al. 2013, *Research in Astronomy and Astrophysics*, 13, 593
- Wang, X.-b., Gu, S.-h., Collier Cameron, A., et al. 2014, *The Astronomical Journal*, 147, 92

- Wang, X.-Y., Wang, S., Hinse, T. C., et al. 2018b, Publications of the Astronomical Society of the Pacific, 130, 064401
- Wang, X.-Y., Wang, Y.-H., Wang, S., et al. 2021, The Astrophysical Journal Supplement Series, 255, 15
- Wang, Y.-H., Wang, S., Liu, H.-G., et al. 2017, The Astronomical Journal, 154, 49
- Wilson, J., Gibson, N. P., Lothringer, J. D., et al. 2021, Monthly Notices of the Royal Astronomical Society, 503, 4787
- Wu, D.-H., Zhang, R. C., Zhou, J.-L., & Steffen, J. H. 2019, Monthly Notices of the Royal Astronomical Society, 484, 1538
- Xie, J.-W., Wu, Y., & Lithwick, Y. 2014, The Astrophysical Journal, 789, 165
- Yee, S. W., Winn, J. N., Knutson, H. A., et al. 2020, Astrophysical Journal Letters, 888, L5
- Zhu, W., Petrovich, C., Wu, Y., Dong, S., & Xie, J. 2018, The Astrophysical Journal, 860, 101